metals

MDPI

Article

Coaxial Electrospinning of $CoS_{1.097}$@C Core–Shell Fibers Anode Material for High-Performance Sodium-Ion Batteries

Hongming Chen [1,2], Yan Li [1,2] and Dan Zhou [1,2,*]

[1] Beijing Advanced Innovation Center for Materials Genome Engineering, University of Science and Technology Beijing, Beijing 100083, China; chenhongming@ustb.edu.cn (H.C.); m202111446@xs.ustb.edu.cn (Y.L.)
[2] Shunde Innovation School, University of Science and Technology Beijing, Foshan 528000, China
* Correspondence: zhoudan@ustb.edu.cn

Abstract: As an important component that affects the storage performance of sodium-ion batteries (SIBs), novel anode materials still need to be well explored. Herein, $CoS_{1.097}$@C core–shell fibers as anode material were designed via coaxial electrospinning, stabilization, and carbonization. Specially, $CoS_{1.097}$ powders are distributed in the inner shell of carbon fibers, and sufficient pore spaces are present among themselves. The unique encapsulation structure, porous characteristics, and one-dimensional conductive carbon shell can enable the $CoS_{1.097}$@C core–shell fibers' high initial specific capacity, excellent rate capability, and long cycle life. The initial charge and discharge capacities of the electrode at 50 mA g^{-1} are 386.0 and 830.9 mAh g^{-1}, respectively. After 2000 cycles at 500 mA g^{-1}, the discharge capacity is 216.3 mAh g^{-1}. Even at 3000 mA g^{-1}, the rate capacity can be maintained at 83.3 mAh g^{-1}.

Keywords: sodium-ion batteries; anode materials; $CoS_{1.097}$@C core—shell fibers; coaxial electrospinning

Citation: Chen, H.; Li, Y.; Zhou, D. Coaxial Electrospinning of $CoS_{1.097}$@C Core–Shell Fibers Anode Material for High-Performance Sodium-Ion Batteries. *Metals* **2024**, *14*, 351. https://doi.org/10.3390/met14030351

Academic Editor: Branimir N. Grgur

Received: 21 February 2024
Revised: 13 March 2024
Accepted: 15 March 2024
Published: 19 March 2024

1. Introduction

The commercial development of sodium-ion batteries (SIBs) is still hindered by some disadvantages related to the proper selection of electrode materials. Due to the larger ion radius of Na^+ ions (1.02 Å, nearly 30% larger than the radius of Li^+ ions), it often causes structural damage to electrode materials and a decrease in the ion transport rate during cycling, resulting in the weak electrochemical performance of SIBs, including small reversible capacity, poor rate performance, and short cycling life [1–8]. At present, exploring suitable anode materials remains an important direction for the development of SIBs. Among the potential anode materials for SIBs that are currently being studied, transition metal sulfides have attracted significant attention, due to their relatively high conductivity, abundant active reaction sites, good thermal/mechanical stability, and low cost [9–13]. However, during the cycling process, transition metal sulfides are prone to significant volume changes due to the insertion and extraction of Na^+ ions, resulting in rapid capacity degradation and poor cycling stability, thereby deteriorating the storage performance of the battery [14–16]. In addition, effective methods are still needed for the preparation of transition metal sulfides [17,18].

To improve the Na storage performance of transition metal sulfide particles, designing materials with a desired morphology and structure is popularly conducted [19–23] using the following methods: (1) The first method is synthesizing nanostructured transition metal sulfides, thereby increasing the active sites of electrode reactions and shortening the diffusion distance of ions/electrons. Meanwhile, by increasing the ratio between the specific surface area and volume, the absolute volume expansion of the material can be reduced, thereby achieving excellent electrochemical cycling performance. (2) The second method is combing transition metal sulfides with conductive carbon materials to utilize the buffering effect of carbon materials to alleviate their volume expansion during cycling,

thereby maintaining the stability of the electrode structure and achieving stable cycling performance and high reversible capacity. In addition, the high conductivity of carbon materials can also enhance the conductivity of transition metal sulfides, which can enable high-rate performance. (3) The third method is designing porous structures for electrode materials, which can offer reduced ion transport distance, increased storage sites for Na^+ ions, and alleviated volume expansion, achieving efficient sodium ion storage.

In terms of material synthesis, coaxial electrospinning technology has attracted widespread attention, due to its unique advantages [1,24–26]. It can obtain one-dimensional hollow fiber materials with a core–shell structure by reasonably configuring the precursor solutions of the core and shell and using optimized electrospinning parameters (electrospinning speed, electrospinning voltage, electrospinning distance from the needle to the roller, etc.) [24–26]. For example, Zhang et al. [24] synthesized hollow Mo_2C@C core–shell nanofibers as anode material for lithium-ion batteries using coaxial electrospinning with reasonable parameters. If coaxial electrospinning technology is also used to prepare novel transition metal sulfide/carbon composite materials with a one-dimensional core–shell structure, and rich gaps are present among the transition metal sulfide particles, it will deliver promising application potential in SIBs. It can effectively address the problems of capacity decaying, poor cycling stability, and unsatisfactory rate capability of transition metal sulfides during the Na storage process, achieving excellent electrochemical performance.

In this work, a novel $CoS_{1.097}$@C core–shell fibers anode material was designed and prepared by coaxial electrospinning. The core precursor solution was a mixed solution prepared by dispersing $CoS_{1.097}$ and polymethyl methacrylate (PMMA) in N,N-Dimethylformamide/acetone (DMF/Ace) mixed solvent, while the shell precursor solution was formed by dissolving polyacrylonitrile (PAN) in DMF solvent. After coaxial electrospinning, the sample underwent stabilization and carbonization treatments, forming the $CoS_{1.097}$@C core–shell fibers. In these core–shell fibers, the shell was carbon fiber, and the inner core was $CoS_{1.097}$ powders with abundant voids among each other. Based on their unique structural characteristics, the $CoS_{1.097}$@C core–shell fibers suggest high conductivity, abundant active material reaction sites and Na^+ ion transport channels, sufficient release space for $CoS_{1.097}$ to tolerate volume expansion during Na^+ ion insertion, and good structural stability upon repeated cycling. These integrated advantages ensure the $CoS_{1.097}$@C core–shell fibers' excellent electrochemical storage performance as anode material for SIBs.

2. Materials and Methods

2.1. Synthesis of the $CoS_{1.097}$ Powders

Firstly, 50 mL of deionized water and 50 mL of ethylene glycol were evenly mixed in a beaker under continuous stirring. Then, 4.98 g of cobalt acetate and 3.044 g of thiourea were added to the above solution and stirred at 60 °C for another 20 min. Next, the obtained solution was transferred to a reactor for a hydrothermal reaction at 170 °C for 24 h. Subsequently, the reaction product was repeatedly cleaned with acetone and deionized water three times. After cleaning, the residue was placed in a culture dish and dried at 70 °C for 12 h. Finally, the dried sample was sintered at 400 °C for 2 h with a sintering rate of 2 °C min^{-1} under an argon atmosphere to obtain the $CoS_{1.097}$ powders.

2.2. Synthesis of the $CoS_{1.097}$@C Core–Shell Fibers

Firstly, the core and shell solutions were prepared for coaxial electrospinning. For the core solution, 0.3 g of $CoS_{1.097}$ powders and 0.715 g of polymethyl methacrylate (PMMA) powders were dispersed in a mixed solvent of N, N-dimethylformamide (DMF) and acetone (Ace) (where the masses of DMF and Ace were 3 g and 2 g, respectively). The shell solution was obtained by dissolving 0.8 g of polyacrylonitrile (PAN) in 8 mL of N, N-dimethylformamide (DMF) solvent. Then, the core and shell solutions were transferred to 10 mL plastic syringes for coaxial electrospinning. The parameters were set as follows: the voltage was 10 kV; the propulsion speed of the core and shell solutions were 0.75 and 1.0 mL h^{-1}, respectively; the distance from the needle to the roller was 12 cm; and

the speed of the roller was 400 r min^{-1}. After coaxial electrospinning, the sample was subjected to heat treatment to obtain the $CoS_{1.097}$@C core–shell fibers. The heat treatment included two stages. The first was pre-oxidation (stabilization). The sintering temperature was 270 °C, the heating rate was 5 °C min^{-1}, the holding time was 1 h, and the sintering atmosphere was air atmosphere. The second was carbonization. The sintering temperature was 500 °C, the heating rate was 5 °C min^{-1}, the holding time was 2 h, and the sintering atmosphere was argon atmosphere.

2.3. Materials Characterization

X-ray diffraction (XRD) patterns were used to analyze the phase of the $CoS_{1.097}$@C core–shell fibers. The Raman spectrum was employed to measure the degree of graphitization of the sample. TG curve was conducted to evaluate the mass ratio of the sample. X-ray photoelectron spectroscopy (XPS) was used to study the surface chemical state of the sample. Scanning electron microscopy (SEM) and transmission electron microscopy (TEM) images were used to observe the morphologies and microstructure of the sample. N_2 adsorption–desorption isotherm curves were taken to investigate the pore structure characteristics (specific surface area, pore volume, and pore distribution) of the sample.

2.4. Electrochemical Measurements

CR2032-type coin cells were used to evaluate the electrochemical performance of the $CoS_{1.097}$@C core–shell fibers. The entire assembly process of cells was conducted in a glove box filled with argon gas. The preparation of the electrode was conducted as follows. $CoS_{1.097}$@C core–shell fibers were firstly mixed with conductive carbon black and Poly(vinylidene fluoride)(PVDF) binder uniformly with a mass ratio of 80%:10%:10% to obtain a uniform slurry. Subsequently, the obtained slurry was coated onto a clean copper foil surface. Then, the copper foil that was coated with slurry was dried (at 100 °C for more than 12 h under vacuum state) to obtain the electrode. Finally, the above electrode was cut into pieces with a diameter of 12 mm for the battery assembly.

When assembling the battery, sodium metal discs with a diameter of 12 mm were used as the reference electrodes/counter electrodes, glass fiber (Whatman, GF/D) was used as the separator, and a 1 M $NaClO_4$ solution (polycarbonate (PC)) solvent containing 5% fluoroethylene carbonate (FEC) additive) was used as the electrolyte. The charging and discharging performances and the curves of Galvanostatic Intermittent Titration Technique (GITT) of the battery were tested using the LAND CT2001A (Wuhan Land Electronics Co., Ltd., Wuhan, China) and CT-4008Tn (Shenzhen Neware Technology Co., Ltd., Shenzhen, China) battery testing systems. The cyclic voltammetry (CV) and impedance performance (EIS) curves of the battery were tested using the CS310H electrochemical workstation (Wuhan Corrtest Instruments Corp., Ltd., Wuhan, China). The voltage windows for the above tests were all in the range of 0.01 and 3.0 V, and the frequency range and amplitude for impedance performance tests were 100 kHz–0.01 Hz and 5 mV, respectively. As a comparative sample, $CoS_{1.097}$ powders were used to prepare electrodes and conduct electrochemical performance tests under the same conditions.

3. Results and Discussion

Figure 1 schematically shows the preparation of the $CoS_{1.097}$@C core—shell fibers. Firstly, $CoS_{1.097}$ and PMMA powders dispersed in a mixed solvent of DMF/Ace and PAN dissolved in DMF solvent were used as the core and shell solutions for coaxial electrospinning, respectively. Then, the above solutions were transferred to the related plastic syringes for coaxial electrospinning. During the coaxial electrospinning process, the core and shell solutions were pushed to the needle with different rates. Due to the unique design of the needle and the slightly higher pushing rate of the shell solution compared to the core solution, the shell solution will form a coating state on the core solution. Because the two solutions have a short convergence time at the needle position, and there is a low diffusion coefficient, they will not be mixed with each other before

solidification. Subsequently, under the role of a high-voltage electric field, hemispherical droplets will form at the needle end and will be further pulled into a Taylor cone core, leading to a jet that is sprayed onto the roller collector covered with tin foil. (During this process, the solvent will quickly evaporate) [27–29]. Thus, raw fibers were initially obtained. Next, the obtained raw fibers were collected and further heat-treated to obtain the final $CoS_{1.097}$@C core–shell fibers. The heat treatment mainly includes two stages. The first stage is pre-oxidation, which gradually stabilizes the PAN in the shell layer and melts the PMMA in the core, thereby obtaining stabilized fibers. The second stage is carbonization, which transforms the PAN in the shell into carbon, and the PMMA in the core is pyrolyzed and burnt off. It should be pointed out that the obtained $CoS_{1.097}$@C core–shell fibers deliver a carbon coating structure, with a shell layer of carbon fiber and an inner layer of $CoS_{1.097}$ powders, and abundant pores exist among the powders due to the burnt-off PMMA. The unique structure of the $CoS_{1.097}$@C core—shell fibers helps the electrode obtain high conductivity, abundant active reaction sites and ion transport channels, and sufficient space for volume expansion of active materials, facilitating high-performance Na storage.

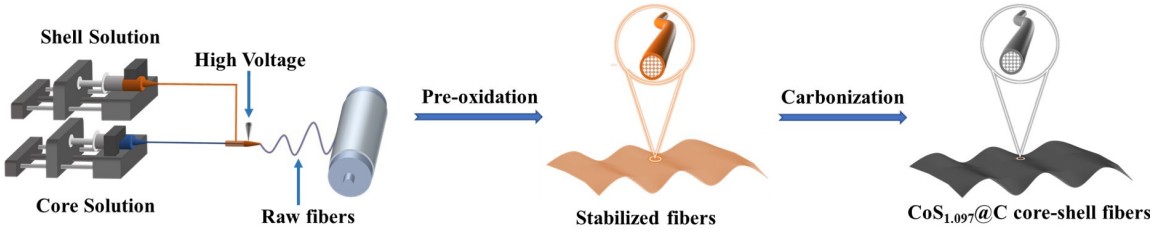

Figure 1. Schematic illustrations of the coaxial electrospinning process of the $CoS_{1.097}$@C core—shell fibers.

The phase and crystal structure of the $CoS_{1.097}$@C core—shell fibers were tested by XRD. As shown in Figure 2a, the characteristic peaks were mainly distributed at 27.9°, 30.9°, 35.6°, 40.0°, 41.1°, 47.0°, 52.4°, 54.6°, and 62.8°, which correspond to the crystal planes of (211), (204), (220), (215), (313), (306), (500), (330), and (1110), respectively. These phase characteristics of the $CoS_{1.097}$@C core—shell fibers are consistent with those of $CoS_{1.097}$ and belong to JCPDS no. 19-0366 [30]. This result indicates that after introducing carbon materials through coaxial electrospinning technology, the main phase of the prepared sample did not change and remained $CoS_{1.097}$. Additionally, the $CoS_{1.097}$ in the core–shell fibers belong to the hexagonal crystal system, with a spatial lattice of P63/mmc (194) and corresponding lattice parameters of a = 10.1 Å, b = 10.1 Å, c = 15.48, $\alpha = \beta = 90.0°$, and $\gamma = 120.0°$. This hexagonal crystal system of $CoS_{1.097}$ has larger lattice channels, which is conducive to achieving larger ion insertion pseudo-capacitance, thereby improving the specific capacity of the electrode [31]. The graphitization degree of the $CoS_{1.097}$@C core—shell fibers was tested using the Raman spectrum. As shown in Figure 2b, there were two distinct peaks located at 1361.9 and 1574.0 cm^{-1}, which belong to the D and G peaks of carbon, respectively. The former represents the degree of disorder and defect of carbon, while the latter indicates the graphitization degree of carbon [32,33]. The intensity ratio (I_D/I_G) of the two peaks was calculated to be 1.32, which indicates that the degree of disorder and defect of carbon in the $CoS_{1.097}$@C core—shell fibers was relatively high, while the degree of graphitization was relatively low. This may be related to the sintering profile of the sample. Generally speaking, the higher the sintering temperature of the sample, the higher the degree of graphitization. In this work, the higher degree of disorder and defects of carbon in the sample can provide more contact sites and reactive sites for the storage of Na^+ ions, benefiting the achievement of high storage capacity [32,33]. In addition, there were some smaller peaks below 700 cm^{-1}, which may be attributed to the contained $CoS_{1.097}$ in the $CoS_{1.097}$@C core—shell fibers [34]. Figure 2c shows the thermogravimetry (TG) curve of the $CoS_{1.097}$@C core—shell fibers. The sample was heated from ambient temperature to 900 °C, with a ramping rate of 10 °C min^{-1} under air atmosphere. It can be

seen that there was a continuous mass decrease before about 700 °C, which can be assigned to the burnt-out contained water and carbon species in the $CoS_{1.097}$@C core—shell fibers. In the following heating process, the mass of the sample tended to be stable, corresponding to the residue of $CoS_{1.097}$ in the $CoS_{1.097}$@C core—shell fibers. Therefore, the mass ratio of $CoS_{1.097}$ in the $CoS_{1.097}$@C core—shell fibers can be calculated to be about 62.7 wt%.

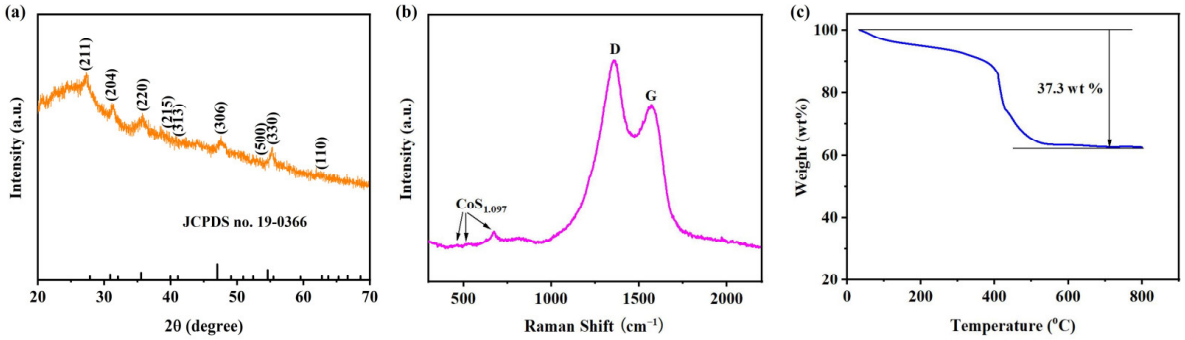

Figure 2. (**a**) XRD patterns, (**b**) Raman spectra, and (**c**) TG curve of the $CoS_{1.097}$@C core—shell fibers.

XPS spectra were collected to analyze the surface chemical states of the $CoS_{1.097}$@C core—shell fibers. Figure 3a shows the full XPS spectrum of the sample. It can be seen that the main elements contained in the sample were C, S, Co, N, O, etc., which is consistent with the design, where the sample mainly included $CoS_{1.097}$ and carbon. Figure 3b shows the high-resolution XPS spectrum of C 1s. As mentioned above, the C in the sample was mainly converted from the polyacrylonitrile precursor. The C 1s spectrum mainly consisted of three peaks located at 283.6 eV, 284.5 eV, and 285 eV, which belong to C–C, C–N, and C–O, respectively [35]. Figure 3c shows the high-resolution XPS spectrum of S 2p. The S in the sample is mainly related to the thiourea precursor. It can be seen that the S 2p spectrum mainly consisted of four peaks located at 160.8 eV, 162.5 eV, 163.0 eV, and 167.9 eV, respectively. These four peaks mainly come from the Co–S, C–S–C, C=S, and SO_{x-} of sulfur [36]. Figure 3d shows the high-resolution XPS spectrum of Co 2p. The Co in the sample mainly comes from the cobalt acetate precursor. The Co 2p spectrum mainly consisted of six peaks located at 780.7 eV, 783.8 eV, 786.8 eV, 796.9 eV, 801.0 eV, and 803.8 eV, respectively. Among them, the first three peaks were mainly Co^{3+} $2p_{3/2}$, Co^{2+} $2p_{3/2}$, and their satellite peaks of Co, while the last three peaks corresponded to Co^{3+} $2p_{1/2}$, Co^{2+} $2p_{1/2}$, and their satellite peaks [37]. Figure 3e shows the high-resolution XPS spectrum of N 1s. The N in the sample also comes from the polyacrylonitrile precursor. The N 1s spectrum can be divided into three peaks, located at 397.7 eV, 399.1 eV, and 400.0 eV, respectively. These three peaks are related to the pyridinic-N, pyrrolic-N, and graphitic-N of nitrogen, which are pyridine nitrogen, pyrrole nitrogen, and graphite nitrogen [33,38]. It should be pointed out that the presence of a certain nitrogen in the active material is beneficial to the improvement of the electrochemical performance of the electrode. On the one hand, it can effectively enhance the conductivity of active materials and promote the rapid transfer of charges. On the other hand, it can effectively increase the number of defects in the active material, thereby enriching the active reaction sites and channels, improving the storage capacity and charge transfer capability of the electrode [33,38]. Figure 3f shows the high-resolution XPS spectrum of O 1s. The O in the sample is possibly related to the air exposure during the sample preparation, which may introduce a small amount of O pollution, such as the water vapor immersion (denoted as O_m). In addition, the precursor of polyacrylonitrile may also produce a certain amount of O defects (O_v) during combustion [39]. The O 1s spectrum mainly consisted of two peaks located at 530.8 eV and 532.4 eV, respectively, corresponding to the defect (O_v) of O and the O (O_m) immersed in water vapor, respectively [39].

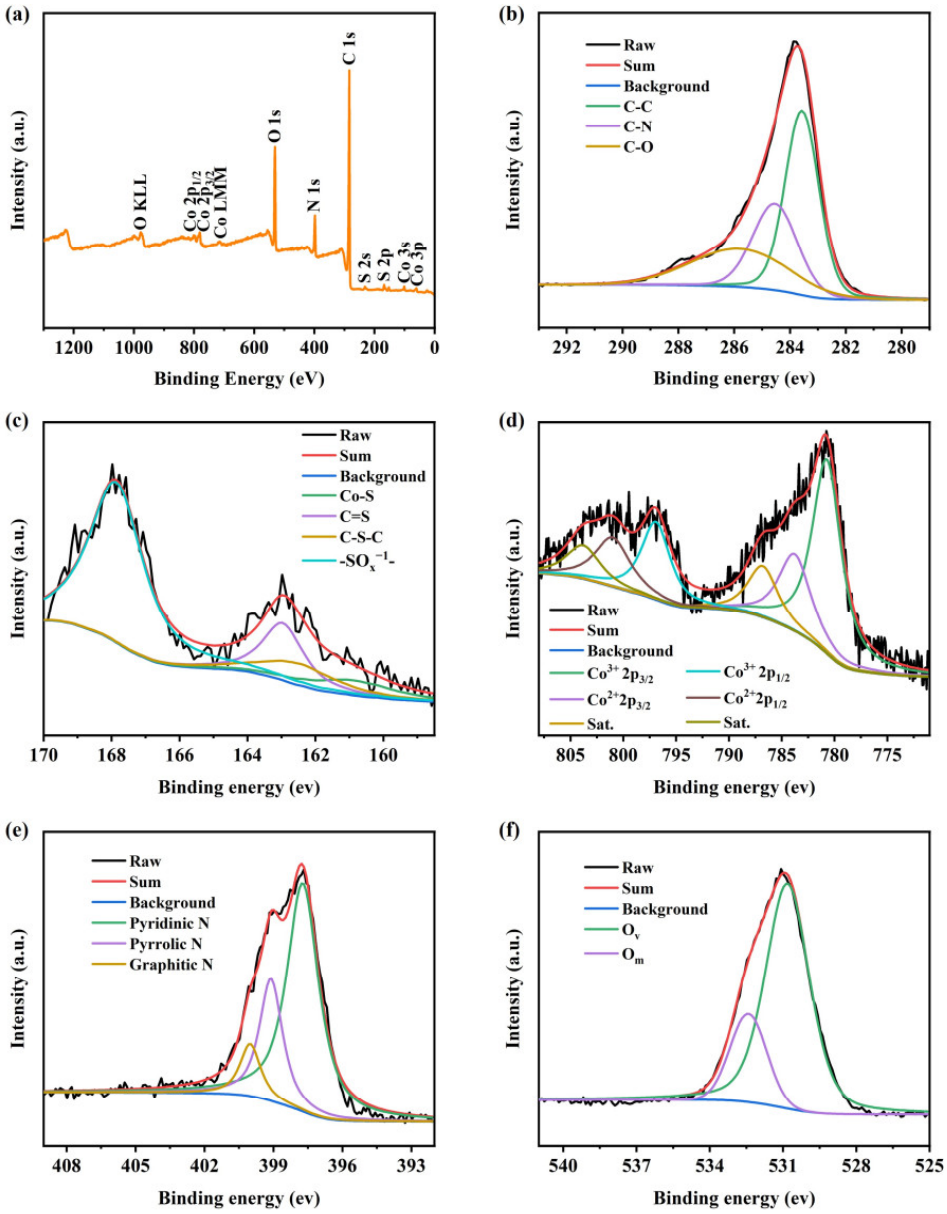

Figure 3. XPS spectrum of the $CoS_{1.097}$@C core—shell fibers. (**a**) Full XPS spectrum, (**b**) high-resolution C 1s spectrum, (**c**) high-resolution S 2p spectrum, (**d**) high-resolution Co 2p spectrum, (**e**) high-resolution N 1s spectrum, and (**f**) high-resolution O 1s spectrum.

Figure 4 shows the SEM images of the $CoS_{1.097}$@C core—shell fibers. It can be seen that the sample suggests a fibrous structure. The diameters of fibers ranged from sub-micrometers to several micrometers. The fibers were generally distributed in a dispersed manner, intertwined or stacked together. Specifically, there was always a series of gourd-like fiber nodes present inside the fibers, which may be related to the conditions during the coaxial electrospinning process. Generally speaking, the viscosity and uniformity of the precursor solution, the setting of electrospinning parameters, the environmental atmosphere, and the heat treatment profile for the fiber synthesis can all affect the morphology of the final sample.

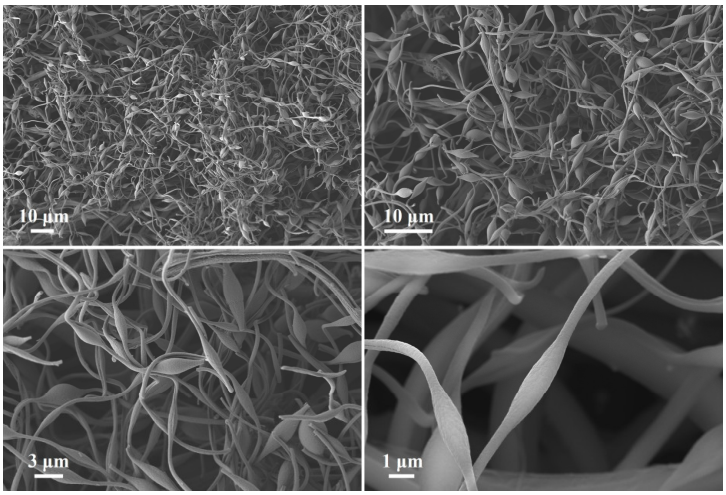

Figure 4. SEM images of the $CoS_{1.097}$@C core—shell fibers under different magnification times.

Figure 5 shows the TEM images of the $CoS_{1.097}$@C core—shell fibers. Clearly, the $CoS_{1.097}$ particles in the prepared fibers were encapsulated in a carbon layer, forming a core–shell structure. Inside the core–shell fibers, there were numerous pores between $CoS_{1.097}$ particles (Figure 5a–c). This structural feature is mainly related to the unique material design via coaxial electrospinning. By means of coaxial electrospinning, $CoS_{1.097}$ and PMMA were encapsulated in PAN fibers. After stabilization and carbonization treatments, PAN fibers were converted into carbon fibers, and PMMA disappeared via pyrolysis, leaving rich pores. Therefore, $CoS_{1.097}$ was distributed inside the carbon fibers, forming the final $CoS_{1.097}$@C core–shell fibers. Figure 5d further verifies this structure feature, and it can be clearly seen that the outer layer of the fiber was a certain thickness of carbon.

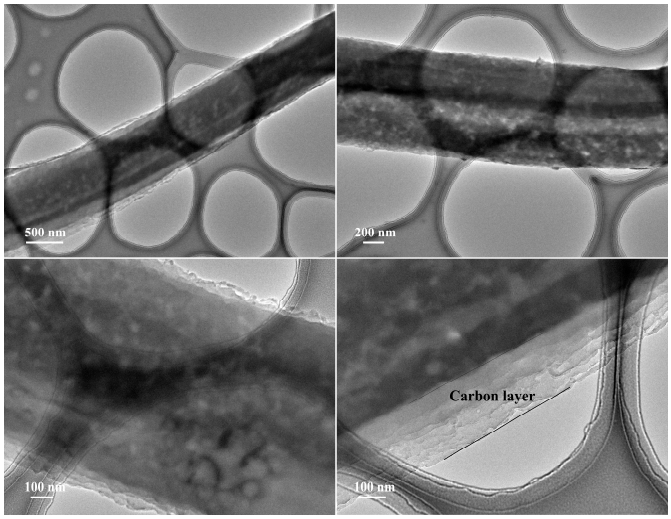

Figure 5. TEM images of the $CoS_{1.097}$@C core—shell fibers under different magnification times.

To further investigate the pore structure characteristics of the $CoS_{1.097}$@C core—shell fibers, the specific surface area and pore distribution of the sample were analyzed. Figure 6a shows the N_2 adsorption–desorption isotherms of the $CoS_{1.097}$@C core—shell fibers. The curve was a typical I/IV profile, indicating that the sample mainly contained various types of pores [33]. Based on the Brunauer–Emmett–Teller (BET) method, the specific surface area of the sample was about 11.4 $m^2\ g^{-1}$. Figure 6b shows the pore distribution curve of the sample via the Barrett–Joyner–Halenda (BJH) method. It can be seen that the pores in the sample included micropores, mesopores, and macropores. Among them, the vast majority

of pores were mesopores (2–50 nm). As reported, the presence of pores can effectively increase the specific surface area and the ion transport channels of the sample and enrich the active sites for the reaction with Na^+ ions, thereby achieving high Na storage capacity and enhanced transport kinetics [32,33]. In addition, the pores in the core–shell fibers were mainly distributed among the $CoS_{1.097}$ particles that encapsulated into carbon fibers, which can provide space for the volume expansion of the $CoS_{1.097}$ active material during the cycling process, effectively maintaining the structure stability and improving the cycling life of the electrode material [32,33].

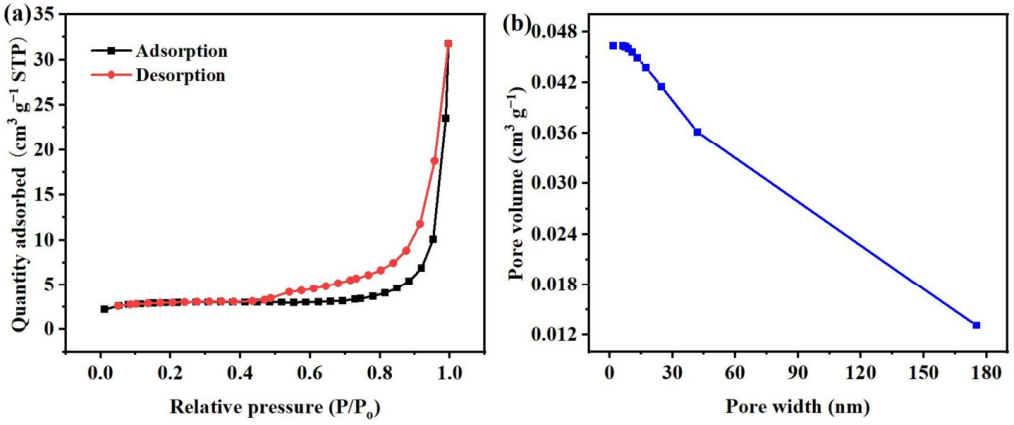

Figure 6. Pore structure characteristics of the $CoS_{1.097}$@C core—shell fibers: (**a**) N_2 adsorption–desorption isotherms, (**b**) pore size distribution curve.

The electrochemical performance of the $CoS_{1.097}$@C core—shell fibers as anode material was studied. Figure 7a shows the CV curves of the sample at a scanning rate of 0.1 mV s^{-1} between the voltage range of 0.01–3.0 V. During the first discharge process, three reduction peaks were observed at 1.1 V, 0.7 V, and 0.3 V, respectively. (The first and third peaks were more prominent, while the second peak was less prominent, with a slower peak pattern.) These three peaks are mainly related to the formation of the irreversible SEI film and the multi-step reaction between Na^+ ions and $CoS_{1.097}$ during the sodification process, resulting in the formation of metallic Co and Na_2S [30,40,41]. During the first charging process, there were three oxidation peaks located at 2.0 V, 1.8 V, and 1.5 V, respectively. (The first and third peaks were not very obvious and had weak intensity, while the second peak was relatively strong.) These three peaks mainly correspond to the reaction between metal Co and Na_2S during the desodification process, accompanying the reversible formation of CoS_x [30,39,40]. In the subsequent cycling process, the changes in the oxidation and reduction peaks of the electrode were relatively consistent, and the CV curves tended to overlap, indicating that the electrode had good reversibility [30,40,41].

Figure 7b shows the charge and discharge curves of the $CoS_{1.097}$@C core—shell fibers at a current density of 50 mA g^{-1}. As can be seen, the initial charging and discharging capacities of the sample were 386.0 and 830.9 mAh g^{-1}, respectively, corresponding to an initial Coulombic efficiency (CE) of 46.5%. The loss of capacity in the initial cycle may be related to the formation of the irreversible SEI film on the surface of active materials [30,40,41]. In the following cycles, the Coulombic efficiency of the electrodes gradually increased, and the charge–discharge curves tended to overlap with each other. This phenomenon indicates that the cycling stability of the electrode was gradually improving, which may be related to the form of the stable SEI film [30,40,41]. Figure 7c shows the comparison of cycling performances between the $CoS_{1.097}$@C core—shell fibers and pure $CoS_{1.097}$ powders at 50 mA g^{-1}. As can be seen, benefiting from the unique microstructure, the $CoS_{1.097}$@C core—shell fibers suggest an improved cycling stability. After 100 cycles, it remained at a discharge capacity of 278.0 mAh g^{-1}. In contrast, the cycling stability of the $CoS_{1.097}$ powders was relatively poor. Additionally, the CE of the $CoS_{1.097}$@C core—shell fibers

was near 100% except for the initial several cycles, indicating the enhanced reversibility of the electrode.

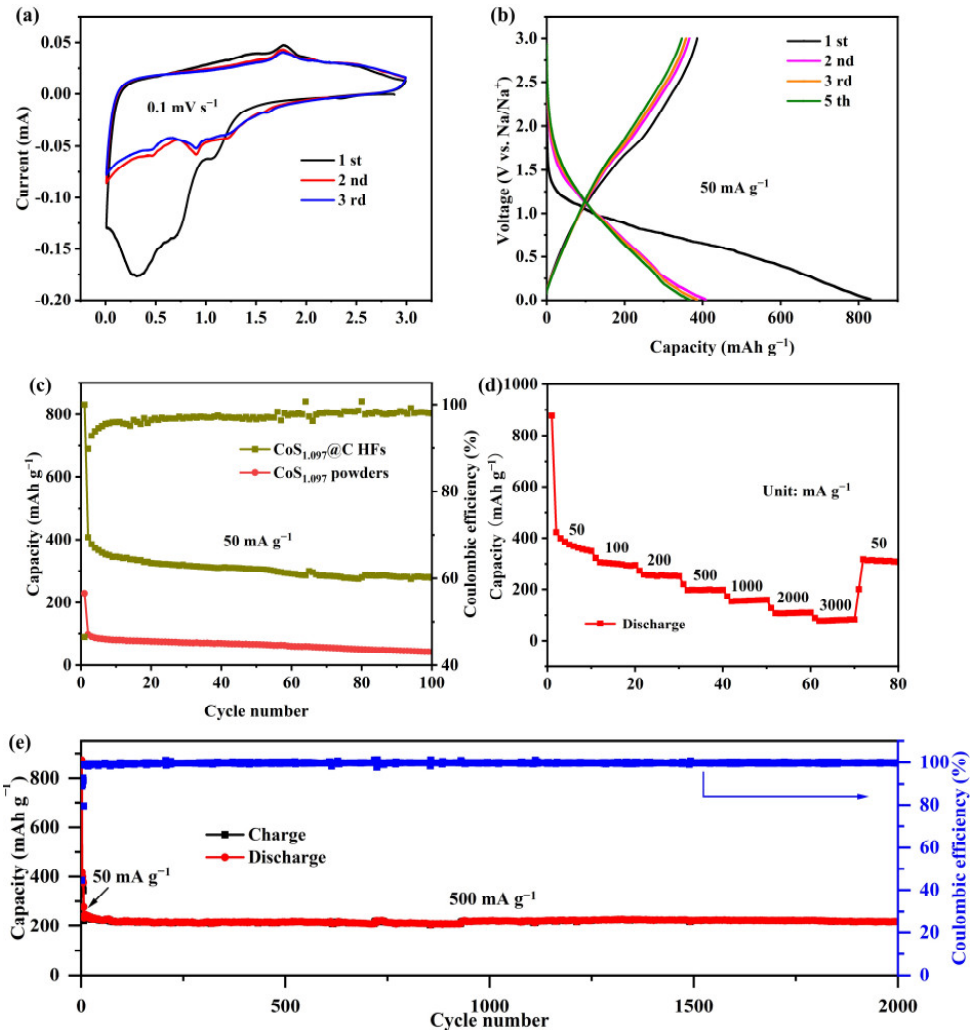

Figure 7. (**a**) CV curves of the $CoS_{1.097}$@C core—shell fibers under the scan rate of 0.1 mV s^{-1}; (**b**) galvanostatic charge–discharge profiles of the $CoS_{1.097}$@C core—shell fibers under 50 mA g^{-1}; (**c**) cycling performance of the $CoS_{1.097}$@C core—shell fibers and $CoS_{1.097}$ powders under 50 mA g^{-1}; (**d**) rate performance of the $CoS_{1.097}$@C core—shell fibers under various current densities; (**e**) long-term cycling performance of the $CoS_{1.097}$@C core—shell fibers under 500 mA g^{-1}.

Figure 7d reveals the rate capability of the $CoS_{1.097}$@C core—shell fibers. At various current densities of 50, 100, 200, 500, 1000, 2000, and 3000 mA g^{-1}, the discharge capabilities were 349.4, 294.6, 251.5, 198.3, 159.7, 109.9, and 83.3 mAh g^{-1}, respectively. Specifically, when the current density returned to 50 mA g^{-1}, it still had a discharge capacity of 307.8 mAh g^{-1}. Compared to the initial capability, the recovery rate was nearly 88.1%. During the whole process of the rate test, the CE of the $CoS_{1.097}$@C core—shell fibers also kept a relatively high level. Additionally, in order to further investigate the long cycling performance of the $CoS_{1.097}$@C core—shell fibers, it was tested under a higher current density of 500 mA g^{-1} (The electrode suffered an activation treatment at the initial 5 cycles under 50 mA g^{-1}). It can be seen that the $CoS_{1.097}$@C core—shell fibers still exhibited an excellent long-term cycling stability, with a large discharge capacity of 216.3 mAh g^{-1} after even 2000 cycles (Figure 7e). Even compared with some reported anode materials for SIBs, the $CoS_{1.097}$@C core—shell fibers also suggested a certain competitiveness, as summarized in Table 1.

Table 1. Comparison of the electrochemical performances of the $CoS_{1.097}$@C core—shell fibers electrodes with some reported anode materials for SIBs.

Sample Name	Current Density	Cycles	Capacity	Ref./Year
Co_9S_8@NPC	50 mA g^{-1}	100	275.3 mAh g^{-1}	[40]/2022
SnS/CNTs	500 mA g^{-1}	100	210 mAh g^{-1}	[42]/2018
ZnS/N-CX	500 mA g^{-1}	270	175 mAh g^{-1}	[43]/2021
CoS_2/rGO	500 mA g^{-1}	100	206 mAh g^{-1}	[44]/2017
$CoS_{1.097}$@C core—shell fibers	50 mA g^{-1}	100	278 mAh g^{-1}	This work
	500 mA g^{-1}	2000	216.3 mAh g^{-1}	

To evaluate the variation in ion transport behavior, EIS curves of the electrode of $CoS_{1.097}$@C core—shell fibers before and after cycling were measured. As shown in Figure 8, both of the curves contained an inclined line in the low-frequency area and a depressed semicircle in the high-frequency area. The former is assigned to Warburg impedance (W) for the diffusion of Na^+ in electrolytes, while the latter is associated with the charge transfer resistance (R_{ct}) at the interface of the electrode and electrolyte. Clearly, the cycled electrode delivers a relative R_{ct} value, corresponding to an enhanced ion transport property during the cycling process.

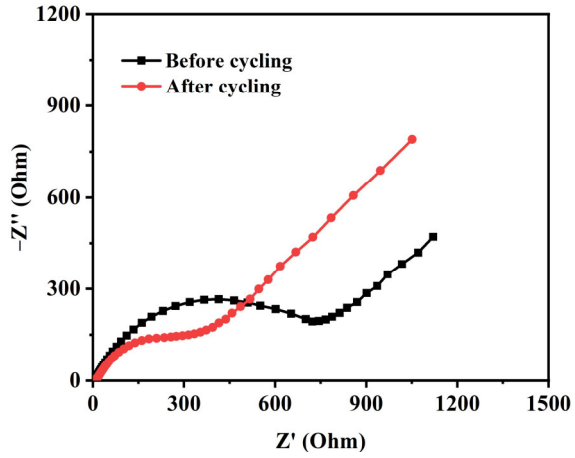

Figure 8. EIS curves of the electrode of $CoS_{1.097}$@C core—shell fibers before and after cycling.

The structural stability of the cycled electrode of $CoS_{1.097}$@C core—shell fibers was investigated. As show in Figure 9, the structure of the $CoS_{1.097}$@C core—shell fibers was relatively rigid, and the fibers almost retained the pristine feature. The enhanced structural stability of the cycled electrode further verifies its excellent long-term cycling performance.

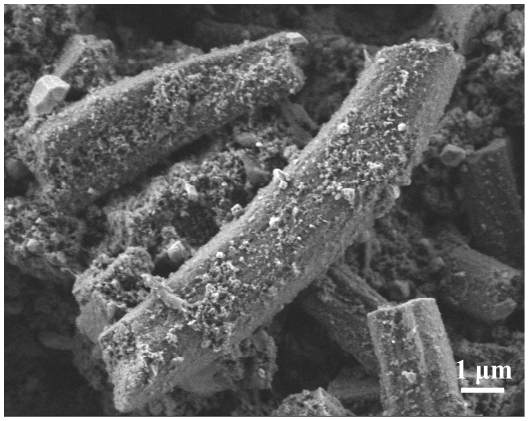

Figure 9. SEM image of the cycled electrode of $CoS_{1.097}$@C core—shell fibers.

4. Conclusions

In summary, a novel anode material of $CoS_{1.097}$@C core–shell fibers was designed via coaxial electrospinning, stabilization, and carbonization. In the inner area of the material, the shell is composed of carbon fibers, with the diameter ranging from sub-micrometers to several micrometers, and the inner core is composed of $CoS_{1.097}$ powders with abundant pores between each other. Benefiting from the unique structure feature, the as-prepared $CoS_{1.097}$@C core–shell fibers suggest high conductivity, abundant active material reaction sites and Na^+ ion transport channels, and sufficient space to accommodate the volume expansion for sodium insertion. Consequently, the $CoS_{1.097}$@C core–shell fibers demonstrate high initial charge and discharge capacities, good rate capability, and excellent, long cycle life. This work provides a feasible design and preparation method for improving the electrochemical performance of transition metal sulfide anode materials, suggesting a promising application potential in the field of SIBs.

Author Contributions: Conceptualization, H.C.; methodology, H.C. and Y.L.; formal analysis, H.C.; validation, Y.L.; investigation, H.C.; data curation, Y.L.; writing—original draft preparation, H.C.; writing—review and editing, D.Z.; supervision, D.Z.; project administration, D.Z. All authors have read and agreed to the published version of the manuscript.

Funding: This research was funded by the Scientific and Technological Innovation Foundation of Shunde Innovation School, USTB, grant number BK21BE010.

Data Availability Statement: The original contributions presented in the study are included in the article, further inquiries can be directed to the corresponding author.

Conflicts of Interest: The authors declare no conflicts of interest.

References

1. Hwang, J.-Y.; Myung, S.-T.; Sun, Y.-K. Sodium-ion batteries: Present and future. *Chem. Soc. Rev.* **2017**, *46*, 3529–3614. [CrossRef]
2. Vaalma, C.; Buchholz, D.; Weil, M.; Passerini, S. A cost and resource analysis of sodium-ion batteries. *Nat. Rev. Mater.* **2018**, *3*, 18013. [CrossRef]
3. Abraham, K.M. How comparable are sodium-ion batteries to lithium-ion counterparts? *ACS Energy Letters* **2020**, *5*, 3544–3547. [CrossRef]
4. Wang, Y.; Xiao, R.; Hu, Y.-S.; Avdeev, M.; Chen, L. P2-$Na_{0.6}[Cr_{0.6}Ti_{0.4}]O_2$ cation-disordered electrode for high-rate symmetric rechargeable sodium-ion batteries. *Nat. Commun.* **2015**, *6*, 6954. [CrossRef]
5. Niu, Y.B.; Guo, Y.J.; Yin, Y.X.; Zhang, S.Y.; Wang, T.; Wang, P.; Xin, S.; Guo, Y.G. High-efficiency cathode sodium compensation for sodium-ion batteries. *Adv. Mater.* **2020**, *32*, 2001419. [CrossRef] [PubMed]
6. Kong, F.; Han, Z.; Tao, S.; Qian, B. Core-shell structured SnSe@C microrod for Na-ion battery anode. *J. Energy Chem.* **2021**, *55*, 256–264. [CrossRef]
7. Pi, Y.Q.; Gan, Z.W.; Yan, M.Y.; Pei, C.Y.; Yu, H.; Ge, Y.W.; An, Q.Y.; Mai, L.Q. Insight into pre-sodiation in Na3V2(PO4)2F3/C @ hard carbon full cells for promoting the development of sodium-ion battery. *Chem. Eng. J.* **2021**, *413*, 127565. [CrossRef]
8. Zhang, H.; Huang, Y.; Ming, H.; Cao, G.P.; Zhang, W.F.; Ming, J.; Chen, R.J. Recent. advances in nanostructured carbon for so-dium-ion batteries. *J. Mater. Chem. A* **2020**, *8*, 1604. [CrossRef]
9. Zheng, F.; Wei, Z.; Xia, H.; Tu, Y.; Meng, X.; Zhu, K.; Zhao, J.; Zhu, Y.; Zhang, J.; Yang, Y.; et al. 3D MoS_2 foam integrated with carbon paper as binder-free anode for high performance sodium-ion batteries. *J. Energy Chem.* **2021**, *65*, 26–33. [CrossRef]
10. Fan, S.; Huang, S.; Chen, Y.; Shang, Y.; Wang, Y.; Kong, D.; Pam, M.E.; Shi, L.; Lim, Y.W.; Shi, Y.; et al. Construction of complex NiS multi-shelled hollow structures with enhanced sodium storage. *Energy Storage Mater.* **2019**, *23*, 17–24. [CrossRef]
11. Zhu, T.; Xiao, Y.; Ren, Y.F.; Zeng, W.; Pan, A.Q.; Zheng, Y.Y.; Liu, Q.B. Unusual formation of CoS0.61Se0.25 anion solid solution with sulfur defects to promote electrocatalytic water reduction. *ACS Appl. Energy Mater.* **2021**, *4*, 2976–2982. [CrossRef]
12. Zhao, J.; Wang, G.L.; Cheng, K.; Ye, K.; Zhu, K.; Yan, J.; Cao, D.X.; Wang, H.E. Growing NiS_2 nanosheets on porous carbon mi-crotubes for hybrid sodium-ion capacitors. *J. Power Sources* **2020**, *451*, 227737. [CrossRef]
13. Ren, J.; Shen, M.; Li, Z.; Yang, C.; Liang, Y.; Wang, H.-E.; Li, J.; Li, N.; Qian, D. Towards high-performance all-solid-state asymmetric supercapacitors: A hierarchical doughnut-like Ni_3S_2@PPy core−shell heterostructure on nickel foam electrode and density functional theory calculations. *J. Power Sources* **2021**, *501*, 230003. [CrossRef]
14. Wang, L.Q.; Han, Z.L.; Zhao, Q.Q.; Yao, X.Y.; Zhu, Y.Q.; Ma, X.L.; Wu, S.D.; Cao, C.B. Engineering yolk-shell P-doped NiS2/C spheres via a MOF-template for high-performance sodium-ion batteries. *J. Mater. Chem. A* **2020**, *8*, 8612–8619. [CrossRef]
15. Ru, J.; He, T.; Chen, B.; Feng, Y.; Zu, L.; Wang, Z.; Zhang, Q.; Hao, T.; Meng, R.; Che, R.; et al. Covalent assembly of MoS_2 nanosheets with SnS nanodots as linkages for lithium/sodium-ion batteries. *Angew. Chem. Int. Ed.* **2020**, *59*, 14621–14627. [CrossRef] [PubMed]

16. Ye, H.L.; Wang, L.; Deng, S.; Zeng, X.Q.; Nie, K.Q.; Duchesne, P.N.; Wang, B.; Liu, S.; Zhou, J.H.; Zhao, F.P.; et al. Amorphous MoS_3 infiltrated with carbon nanotubes as an advanced anode material of sodium-ion batteries with large gravimetric, areal, and volumetric capacities. *Adv. Energy Mater.* **2016**, *7*, 1601602. [CrossRef]
17. Yang, D.; Chen, W.; Zhang, X.; Mi, L.; Liu, C.; Chen, L.; Guan, X.; Cao, Y.; Shen, C. Facile and scalable synthesis of low-cost FeS@C as long-cycle anodes for sodium-ion batteries. *J. Mater. Chem. A* **2019**, *7*, 19709–19718. [CrossRef]
18. Wang, F.; Zhang, W.; Zhou, H.; Chen, H.; Huang, Z.; Yan, Z.; Jiang, R.; Wang, C.; Tan, Z.; Kuang, Y. Preparation of porous FeS2-C/RG composite for sodium ion batteries. *Chem. Eng. J.* **2020**, *380*, 122549. [CrossRef]
19. Chen, S.; Li, G.; Yang, M.; Xiong, J.; Akter, S.; Mi, L.; Li, Y. Nanotube assembled coral-like ZnS@N, S co-doped carbon: A sodium-ion batteries anode material with outstanding stability and rate performance. *Appl. Surf. Sci.* **2021**, *535*, 147748. [CrossRef]
20. Wang, Y.; Wang, Y.; Feng, X.; Chen, W.; Qian, J.; Ai, X.; Yang, H.; Cao, Y. In Situ Formation of Co_9S_8 Nanoclusters in Sulfur-Doped Carbon Foam as a Sustainable and High-Rate Sodium-Ion Anode. *ACS Appl. Mater. Interfaces* **2019**, *11*, 19218–19226. [CrossRef]
21. Li, X.Y.; Li, K.K.; Zhu, S.C.; Fan, K.; Lyu, L.L.; Yao, H.M.; Li, Y.Y.; Hu, J.L.; Huang, H.T.; Mai, Y.-W.; et al. Fi-ber-in-tube design of Co9S8-Carbon/Co9S8: Enabling efficient sodium storage. *Angew. Chem. Int. Ed.* **2019**, *58*, 6239–6243. [CrossRef]
22. Luo, Y.Y.; Shi, L.D.; He, H.Z.; Cong, G.T.; Zhu, C.Z.; Xu, J. Rationally designed yolk-shell Co9S8-Co1-xS hollow spheres for advanced sodium-ion storage. *J. Mater. Chem. A* **2021**, *9*, 23537–23544. [CrossRef]
23. Lian, Y.J.; Chen, F.J.; Kang, H.Y.; Wu, C.X.; Zhang, M.; Xu, S.L. Co_9S_8 nanoparticles scaffolded within car-bon-nanoparticles-decorated carbon spheres as anodes for lithium and sodium storage. *Appl. Surf. Sci.* **2020**, *507*, 145061. [CrossRef]
24. Zhang, M.; Huang, X.; Xin, H.; Li, D.; Zhao, Y.; Shi, L.; Lin, Y.; Yu, J.; Yu, Z.; Zhu, C.; et al. Coaxial electrospinning synthesis hollow Mo2C@C core-shell nanofibers for high-performance and long-term lithium-ion batteries. *Appl. Surf. Sci.* **2019**, *473*, 352–358. [CrossRef]
25. Li, L.L.; Peng, S.J.; Lee, J.K.Y.; Ji, D.X.; Srinivasan, M.; Ramakrishna, S. Electrospun hollow nanofibers for advanced secondary batteries. *Nano Energy* **2017**, *39*, 111–139. [CrossRef]
26. Li, X.; Chen, W.; Qian, Q.; Huang, H.; Chen, Y.; Wang, Z.; Chen, Q.; Yang, J.; Li, J.; Mai, Y.-W. Electrospinning-Based Strategies for Battery Materials. *Adv. Energy Mater.* **2021**, *11*, 2000845. [CrossRef]
27. Wang, J.; Wang, Z.; Ni, J.; Li, L. Electrospinning for flexible sodium-ion batteries. *Energy Storage Mater.* **2022**, *45*, 704–719. [CrossRef]
28. Jung, J.-W.; Lee, C.-L.; Yu, S.; Kim, I.-D. Electrospun nanofibers as a platform for advanced secondary batteries: A comprehensive review. *J. Mater. Chem. A* **2016**, *4*, 703–750. [CrossRef]
29. Wang, H.-G.; Yuan, S.; Ma, D.-L.; Zhang, X.-B.; Yan, J.-M. Electrospun materials for lithium and sodium rechargeable batteries: From structure evolution to electrochemical performance. *Energy Environ. Sci.* **2015**, *8*, 1660–1681. [CrossRef]
30. Li, A.; Xiong, P.; Zhang, Y.; Shuang, W.; Chang, Z.; Xu, Y.; Bu, X.-H. 2D MOF-derived CoS1.097 nanoparticle embedded S-doped porous carbon nanosheets for high performance sodium storage. *Chem. Eng. J.* **2021**, *405*, 126638. [CrossRef]
31. Jia, J.; Liu, X.; Mi, R.; Liu, N.; Xiong, Z.; Yuan, L.; Wang, C.; Sheng, G.; Cao, L.; Zhou, X.; et al. Self-assembled pancake-like hexagonal tungsten oxide with ordered mesopores for supercapacitors. *J. Mater. Chem. A* **2018**, *6*, 15330–15339. [CrossRef]
32. Zhou, D.; Fan, L.-Z. Co_2P nanoparticles encapsulated in 3D porous N-doped carbon nanosheet networks as an anode for high-performance sodium-ion batteries. *J. Mater. Chem. A* **2018**, *6*, 2139–2147. [CrossRef]
33. Zhou, D.; Yi, J.; Zhao, X.; Yang, J.; Lu, H.; Fan, L.-Z. Confining ultrasmall CoP nanoparticles into nitrogen-doped porous carbon via synchronous pyrolysis and phosphorization for enhanced potassium-ion storage. *Chem. Eng. J.* **2021**, *413*, 127508. [CrossRef]
34. Zhang, J.Y.; Sun, L.P.; Kong, F.H.; Huo, L.H.; Zhao, H. Architecture of porous $CoS_{1.097}$-C composite nanowire for efficient oxygen reduction reaction. *Int. J. Hydrogen Energy* **2019**, *44*, 3681–3689.
35. Luo, Q.; Wen, J.X.; Liu, G.Z.; Ye, Z.Q.; Wang, Q.F.; Liu, L.; Yang, X.K. Sb_2Se_3/Sb embedded in carbon nanofibers as flexible and twistable anode for potassium-ion batteries. *J. Power Sources* **2022**, *545*, 231917. [CrossRef]
36. Peng, W.; Wang, Y.; Yang, X.; Mao, L.; Jin, J.; Yang, S.; Fu, K.; Li, G. Co9S8 nanoparticles embedded in multiple doped and electrospun hollow carbon nanofibers as bifunctional oxygen electrocatalysts for rechargeable zinc-air battery. *Appl. Catal. B Environ.* **2020**, *268*, 118437. [CrossRef]
37. Wang, J.; Zhao, S.; Xian, X. Co9S8@partly-graphitized carbon composites obtained through catalytic graphitization strategy as anode materials for lithium-ions batteries. *J. Electroanal. Chem.* **2021**, *897*, 115569. [CrossRef]
38. Zang, R.; Li, P.; Guo, X.; Man, Z.; Zhang, S.; Wang, C.; Wang, G. Yolk–shell N-doped carbon coated FeS_2nanocages as a high-performance anode for sodium-ion batteries. *J. Mater. Chem. A* **2019**, *7*, 14051–14059. [CrossRef]
39. Wei, C.; Han, Y.; Liu, H.; Gan, R.; Ma, W.; Liu, H.; Song, Y.; Zhang, X.; Shi, J.; Ma, C. Enhancing conversion of polysulfides via porous carbon nanofiber interlayer with dual-active sites for lithium-sulfur batteries. *J. Colloid. Interface Sci.* **2022**, *625*, 946–955. [CrossRef]
40. Chen, H.; Niu, Y.; Meng, Y.; Ren, X.; Huang, Y.; Wang, M.; Lau, W.-M.; Zhou, D. Constructing nitrogen-doped porous carbon immobilized Co9S8 composite as high-performance anode material for sodium-ion batteries. *J. Alloy. Compd.* **2022**, *923*, 166373. [CrossRef]
41. Zhao, W.; Ma, X. Direct growth of flower-shaped CoS1.097 nanoflakes on flexible carbon cloth: An ultrastable cycle durability anode for reversible sodium storage. *Scr. Mater.* **2020**, *186*, 114–120. [CrossRef]
42. Chen, Y.; Wang, B.; Hou, T.; Hu, X.; Li, X.; Sun, X.; Cai, S.; Ji, H.; Zheng, C. Enhanced electrochemical performance of SnS nanoparticles/CNTs composite as anode material for sodium-ion battery. *Chin. Chem. Lett.* **2018**, *29*, 187–190. [CrossRef]

43. Tian, G.; Song, Y.; Luo, X.; Zhao, Z.; Han, F.; Chen, J.; Huang, H.; Tang, N.; Dsoke, S. ZnS nanoparticles embedded in N-doped porous carbon xerogel as electrode materials for sodium-ion batteries. *J. Alloy. Compd.* **2021**, *877*, 160299. [CrossRef]
44. Xie, K.Y.; Li, L.; Deng, X.; Zhou, W.; Shao, Z.P. A strongly coupled CoS_2/ reduced graphene oxide nanostructure as an anode material for efficient sodium-ion batteries. *J. Alloys Compd.* **2017**, *726*, 394–402. [CrossRef]